PHYSICAL REVIEW APPLIED **19,** 054057 (2023)

Numerical Simulation of the Radiation Force from Transient Acoustic Fields: Application to Laser-Guided Acoustic Tweezers

Shuhan Chen, Qing Wang,[‡] Qi Wang, Jia Zhou,[*] and Antoine Riaud[†,§]
State Key Laboratory of ASIC and System, School of Microelectronics, Fudan University, Shanghai 200433, China

(Received 11 January 2023; revised 21 March 2023; accepted 21 April 2023; published 17 May 2023)

Using pulsed acoustic waves could provide a superior selectivity for microscale acoustic tweezers. However, the theory for the radiation force of pulsed acoustic waves has only been recently derived and no numerical implementations are available. In this paper, we present a finite-element implementation of this model to simulate the transient acoustic radiation force on small spheres. We use the model to simulate laser-guided acoustic tweezers and optimize their performance. By enabling numerical simulations of the transient radiation force, this work may accelerate the rational design of pulse-based high-selectivity acoustic tweezer devices.

DOI: 10.1103/PhysRevApplied.19.054057

I. INTRODUCTION

Acoustic radiation force (ARF), a steady force generated by acoustic waves, is a convenient means to achieve micro-object manipulation, such as microsample separation [1–3] and enrichment [4], cell sorting [5,6], and single-cell manipulation [7].

Using transient excitation such as pulses and wave trains could enable much more precise manipulation than when using time-periodic acoustic fields [1–7]. First, pulsed acoustic manipulation is less disturbed by Rayleigh acoustic streaming [8,9] because the radiation force is established much faster than streaming [10,11]. Second, the use of acoustic wave packets allows the localization of the acoustic interference patterns and thus the control of the spatial extent of the acoustic trapping region [12]. Indeed, standing waves exert much larger radiation forces than traveling waves (in the small particle limit), allowing the acoustic field outside the interference region to be neglected. Laser-guided acoustic tweezers (LGATs) [13] exploit this interference principle to create a hybridized radiation force landscape that couples a high-amplitude piezogenerated acoustic field (strong, *Z* field) and a light-patterned photogenerated acoustic field (weak, *L* field). The hybridized field retains the spatial information of the *L* field and the strength of the *Z* field.

Despite these promises of reduced streaming and higher selectivity, theoretical and numerical studies of transient acoustic fields are still rare. A typical example of the limited current understanding of transient nonlinear acoustics is the suppression of acoustic streaming by acoustic pulses [8,9], where the only model available for transient streaming [14] has been unable to qualitatively explain experimental observations [10,11]. Similarly, there are no numerical schemes to study transient ARF directly without solving the full nonlinear compressible Navier-Stokes equation [15,16], which has a potentially significant overhead.

In this paper, we implement the recent generalization of the radiation force theory for small spheres (Gor'kov theory [17]) to transient acoustic fields [18]. In addition to requiring that the objects be spherical and much smaller than the acoustic wavelength in the bandwidth considered, this theory ignores microstreaming and would not be suitable for studying very dense particles in highly viscous fluids (such as copper in glycerol [19]). It also requires that scattering events do not overlap, so extreme care must be taken when investigating the response of bubbles or other high-quality acoustic resonators. Nevertheless, the underlying assumptions suggest that the theory is valid for cells or plastic particles immersed in water.

The paper is arranged as follows. After summarizing the theory of the dynamic acoustic radiation force, Sec. II details a numerical implementation of the dynamic ARF and details the model setup for the simulation of a LGAT. In Sec. III, the acoustic field in a LGAT device is briefly presented, and then the resulting ARF is analyzed depending on the particle location and the phase difference between the laser and the piezoelectric. Then, the excitation parameters of the LGAT (pulse duration and laser beam width) are optimized to maximize the ARF.

---

[*] jia.zhou@fudan.edu.cn

[†] antoine_riaud@fudan.edu.cn

[‡] Current affiliation: Department of Biomedical Engineering, Lund University, Ole Römers väg 3, Lund 22363, Sweden.

[§] Current affiliation: ABB Corporate Research Center, Baden-Dättwil, Switzerland.

II. THEORIES AND METHODS

A. Transient ARF: governing equations

Our simulations implement the theory of ARF on small rigid spheres in transient acoustic fields of Wang *et al.* [18]. Similar to most other radiation pressure theories, the peak pressure amplitude of the wave $p_{\max}$ is assumed to be small such that $p_{\max}/\rho_0 c_0^2 = \epsilon \ll 1$, where ϵ is the acoustic Mach number and ρ_0 is the quiescent fluid density. According to the perturbation method, the fluid quantities can be resolved as

$$p = p_0 + p_1 + p_2, \tag{1a}$$

$$\mathbf{v} = \mathbf{v_0} + \mathbf{v}_1 + \mathbf{v}_2, \tag{1b}$$

$$\rho = \rho_0 + \rho_1 + \rho_2, \tag{1c}$$

where the subscripts 0–2 indicate the perturbation order of each term $q_1 = O(q_0\epsilon)$ and $q_2 = O\left(q_0\epsilon^2\right)$ where q can be any physical field among pressure p, velocity $\mathbf{v}$, and density ρ. Accordingly, time-invariant zero-order terms are interpreted as constant (hydrostatic) contributions, the first-order terms as acoustic contributions, and the second-order terms as the source of nonlinear effects, such as radiation pressure or acoustic streaming. Although radiation force theory requires knowledge of the total acoustic field, Gor'kov theory is conveniently expressed in terms of the incident acoustic field only. Henceforth, all acoustic quantities will refer to the incident field in the remainder of the paper.

Compared to Gor'kov theory, the assumption of single-frequency acoustic fields is extended to wave packets of finite duration τ: all the wave quantities q_1 are required to satisfy the condition $q_1(0, \mathbf{r}) = q_1(\tau, \mathbf{r})$, where $\mathbf{r}$ denotes the position vector and time origin can be chosen arbitrarily. Additionally, the pulse duration must be short enough to neglect the displacement of the sphere compared to the shortest wavelength, which amounts to $1/\tau \gg f_{\max}\epsilon^2$, where $f_{\max}$ refers to the highest frequency in the pulse.

In the case of an inviscid fluid (viscoacoustic and thermoacoustic boundary layers much thinner than the particle diameter [20,21]), the acoustic radiation force reads

$$\mathbf{F}_{\text{rad}} = -V_p \nabla U, \tag{2}$$

with the particle volume $V_p = 4\pi R_p^3/3$ and the generalized Gor'kov potential:

$$U = \langle U_{\text{inst}} \rangle = \frac{1}{t_{\text{tot}}} \int U_{\text{inst}} \mathrm{d}t, \tag{3}$$

where t_{tot} is the duration between wave trains and U_{inst} is interpreted as a fictive (but convenient) instantaneous Gor'kov potential:

$$U_{\text{inst}} = f_1 \mathcal{V} - \frac{3}{2} f_2 \mathcal{K}. \tag{4}$$

Here $\mathcal{V} = p_1^2/(2\rho_0 c_0^2)$ and $\mathcal{K} = \rho_0 \mathbf{v}_1 \cdot \mathbf{v}_1/2$ represent the instantaneous potential energy and kinetic energy, respectively. $f_1 = 1 - \rho_0 c_0^2/(\rho_p c_p^2)$ is the monopole scattering coefficient and $f_2 = 2\left(\rho_p - \rho_0\right)/(2\rho_p + \rho_0)$ is the dipole scattering coefficient.

Therefore, computation of the radiation force requires knowing the incident acoustic field, which can be computed using transient acoustic pressure models:

$$\frac{1}{c_0^2}\frac{\partial^2 p_1}{\partial t^2} - \nabla^2 p_1 = 0, \tag{5}$$

from which the fluid acceleration can be deduced using the Euler equation:

$$\mathbf{a}_1 = -\frac{1}{\rho_0}\nabla p_1, \tag{6}$$

and the velocity

$$\mathbf{v}_1 = \int \mathbf{a}_1 \mathrm{d}t. \tag{7}$$

Under these hypotheses, the general Gor'kov approach can be used to calculate ARF in such transient situations.

B. Transient ARF: numerical implementation

The numerical model for the simulation of hybridized acoustic fields is configured in the commercial finite-element-method software COMSOL Multiphysics version 5.4, and the parameters used are given in Table I. The model uses the "Pressure Acoustics, Transient" module to solve the first-order acoustic pressure field in the fluid domain [Eq. (1b) and to deduce the acceleration and velocity fields with Eq. (7)]. The settings for solving transient waves follow the approach suggested in Ref. [22].

Transient acoustic field studies necessarily involve bandwidth issues. On the one hand, the excitation signal (such as a short laser pulse) may have a very wide bandwidth. On the other hand, the integration of the acoustic partial differential equation is often done with a constant time step and the mesh imposes constraints on the minimum wavelength that can be resolved (that is, the maximum frequency). The Courant-Friedrichs-Lewy (CFL) condition provides guidelines for setting the time step Δt depending on the maximum mesh size h [14,22]:

$$C = \frac{c_0 \Delta t}{h}, \tag{8}$$

where C is called the CFL number. Using the default second-order (quadratic) mesh elements, the recommended C is approximately 0.1. Thus, given a maximum

TABLE I. Summary of simulation parameters.

Electroacoustic wave parameters		
Frequency	f^Z	10 MHz
Velocity magnitude	v_0^Z	1.83 m/s
Number of shots (periods)	n^Z	5
Density	ρ_z	4640 kg/m^3
Laser-induced acoustic wave parameters		
Frequency	f^L	10 MHz
Velocity magnitude	v_0^L	0.6 m/s
Radius of spot waist	R_w	20 μm
Fluid		
Density	ρ_0	1050 kg/m^3
Speed of sound	c_0	1500 m/s
Domain width (radius)	R_d	375 μm
Domain height	h_d	200 μm
Particle		
Density	ρ_p	1050 kg/m^3
Radius	R_p	10 μm
Mesh and solver		
CFL number	C	0.1
Units per local wavelength	N	12
Others		
Simulation time	t_{sim}	2 μs
Duration between wave trains	t_{tot}	20 μs

frequency f_{max} that needs to be resolved, the CFL condition yields the time step $\Delta t = C/(Nf_{\text{max}})$ where N is the number of elements per local wavelength λ. Due to the spatial frequency doubling of the Gor'kov potential (terms in p_1^2 and v_1^2), we choose $N = 12$ instead of the more common $N = 6$ in linear acoustics (a mesh convergence study is available in Appendix A).

Boundary conditions must be carefully designed according to this bandwidth constraint. The most straightforward boundary condition is to directly specify an acceleration that fits in the simulated frequency bandwidth. In some cases, however, it is necessary to specify the velocity instead (e.g., when the velocity is known from laser Doppler vibrometer measurements), which can yield a stepwise acceleration if there is a slope break in the velocity. To address this problem, the input velocity is first multiplied by a smoothing window and then derived to obtain the acceleration boundary condition.

The velocity field [Eq. (7)] is computed by coupling the "Pressure Acoustic" module to a "Distributed Ordinary Differential Equation (DODE)" module in COMSOL with the damping factor set to 1 in DODE.

The first-order velocity is then used to calculate the instantaneous Gor'kov potential U_{inst} via Eq. (4) along with the first-order acoustic pressure. Similarly, Eq. (3) is implemented in the DODE module to obtain U. Finally, the ARF is obtained as the gradient of U (using the COMSOL function `diff()`). Given the small size of the geometry, computer memory is not a constraint in this study, and all the fields are computed using a single fully coupled time-dependent solver for simplicity, but the perturbation approach of the model could allow the use of a segregated solver that solves the fields one after another for each time step.

C. Simulation of a LGAT: initial and boundary conditions

In a LGAT (schematically shown in Fig. 1), two acoustic sources interfere to generate an acoustic trap. A piezoelectric acoustic source (strong field, labeled with the superscript "Z") yields a plane traveling wave of high amplitude, which creates no in-plane acoustic radiation force due to symmetry constraints (the wave is in-plane invariant). This wave interferes with a weaker acoustic wave (weak field, labeled with the superscript "L") generated by the photoacoustic conversion of a laser pulse. The combined incident pressure and velocity fields read $p_1 = p_1^L + p_1^Z$ and $\mathbf{v} = \mathbf{v}_1^L + \mathbf{v}_1^Z$, respectively. According to Eqs. (3) and (4), this yields a Gor'kov potential with cross terms $U = U^{ZZ} + U^{ZL} + U^{LL}$. The vanishing gradient of the spatially invariant U^{ZZ} leads to a negligible in-plane force, while U^{LL} is negligible due to the small photoacoustic conversion efficiency. As a result, only the hybridized potential U^{ZL} dominates, and the force is well approximated by

$$\mathbf{F}_{\text{rad}} = -V_p \nabla U \approx -V_p \nabla U^{ZL} = -V_p \nabla \left\langle U_{\text{inst}}^{ZL} \right\rangle, \quad (9)$$

with $U_{\text{inst}}^{ZL} = f_1 p_1^Z p_1^L/(\rho_0 c_0^2) - (3/2) f_2 \rho_0 \mathbf{v}_1^Z \cdot \mathbf{v}_1^L$. We note that U_{inst} is twice as large as in Eq. (4) due to the binomial coefficients in the expansion of p_1^2 and $\mathbf{v}_1 \cdot \mathbf{v}_1$.

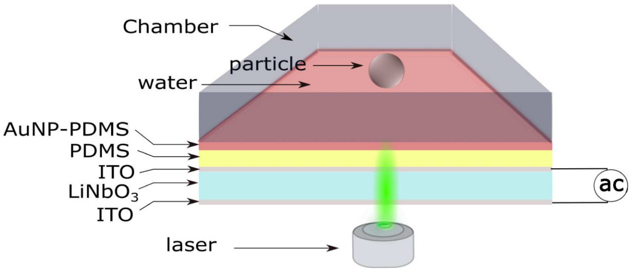

FIG. 1. Laser-guided acoustic tweezer structure. The particle is manipulated by the combination of a weak and a strong acoustic field. The interference between the two fields yields a radiation force with spatial characteristics similar to the weak field but with a much higher amplitude. The L field is generated by the photoacoustic conversion of a pulsed-laser beam on the gold nanoparticle-polydimethylsiloxane (AuNP-PDMS) composite. The composite selectively absorbs green light and is transparent to other wavelengths. The Z field is generated by piezoelectric conversion of an electric signal (ac) in the LiNbO$_3$. The electrodes (indium tin oxide, ITO) are transparent. As a result, the whole device is transparent to most optical wavelengths except green, and the particles under manipulation can be directly visualized.

While we focus mainly on the acoustic radiation pressure, we note that acoustic streaming plays a negligible role in this study due to the particle radius of 25 µm used in the experiments [23]. For fluids in the channel, thermophoresis and thermal agitation can also be factors driving the particles [24]. To rule out this possibility, we turn off the bulk acoustic wave (BAW) from the Z source and observe no motions of particles despite the laser heating [13]. Therefore, thermal effects are also neglected in the model. The other parameter values are given in Table I. Most of these parameters are selected based on the typical experimental values while they are sometimes simplified to facilitate dimensionless analysis [e.g., f^Z is rounded to 10 MHz instead of the exact resonance frequency of the crystal used in experiments (7.6 MHz)]. Furthermore, a key goal of the paper is to estimate what would be the upper limit of the radiation force of the LGAT if suitable laser and electronic excitation were provided. For the electroacoustic field, a simple estimate is obtained by using the definition of the piezoelectric coupling coefficient K^2:

$$\frac{1}{2}C(Ed)^2K^2 \simeq \frac{1}{2}\rho_z A d {v_0^Z}^2, \tag{10}$$

where d is the thickness and A is the area of the dielectric crystal, together with the capacitance $C = (\varepsilon_r\varepsilon_0 A)/d$ and the field strength E. On this basis, an estimation of the velocity is derived as $v_0^Z = KE\sqrt{\varepsilon_r\varepsilon_0/\rho_z}$. This velocity is independent of the excitation frequency and is limited by the coercivity field strength of the crystal, which is of the order of 21 MV/m for LiNbO$_3$ [25]. The Y-36° cut has a $K^2 = 0.1$. For the sake of simplicity, the material anisotropy is overlooked and we consider a relative permittivity of the order of $\varepsilon_r \approx 40$, which yields a maximum velocity of 1.83 m/s.

To satisfy $U^{LL} \ll U^{ZL}$ as required by the hybridized-field theory, the maximum excitation velocity of the photoacoustic field is set to 60 cm/s. We note that the material damage threshold could in principle allow higher velocities. More details about this criterion are given in Appendix B.

Since the laser spot is axisymmetric and the Z wave is spatially invariant, we use a two-dimensional axisymmetric model (cylindrical coordinate system) as shown in Fig. 2(a). We restrict our analysis to a rectangular cross section [purple part in Fig. 2(a)] of width $R_d = n_\lambda \lambda^Z/2 = 375$ µm (with $n_\lambda = 5$) and height $h_d = 200$ µm in the vertical r-z plane for a 10-MHz wave. The width is chosen large enough to ensure that the radiation force decreases to less than 5 % of its maximum value at this distance.

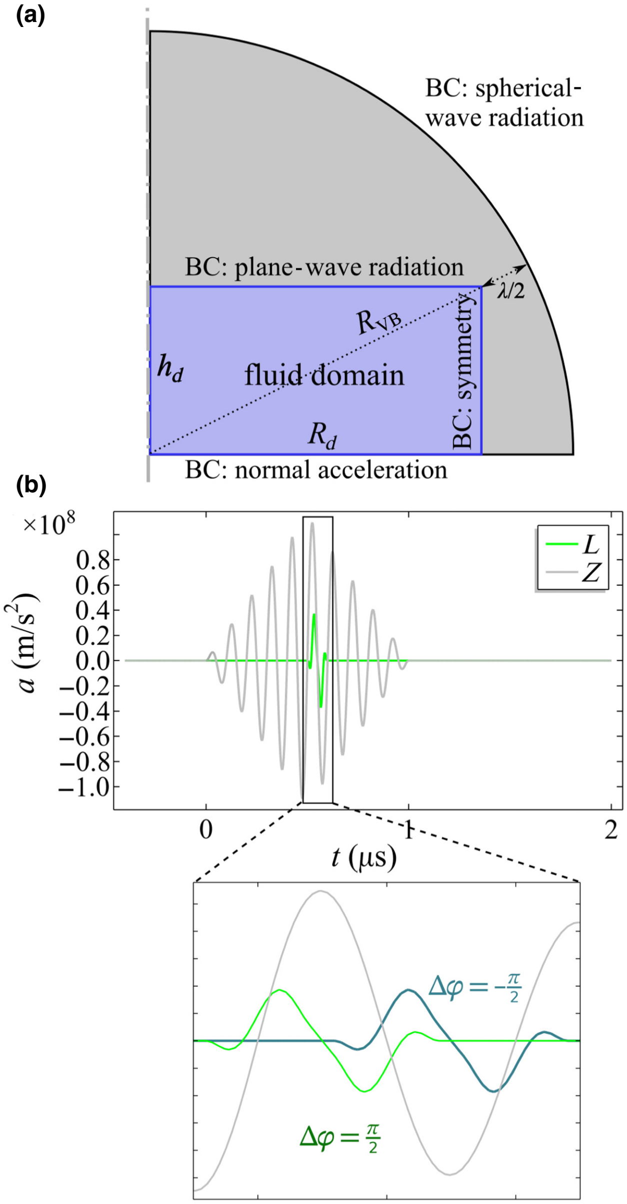

FIG. 2. Model setup. (a) Sketch of the two-dimensional axial symmetry computational domain. The purple domain is used for the simulation of the Z field and the calculation of the radiation force. The gray domain is used for the calculation of the L field. (b) Input signals applied to the bottom boundary. The input signals are depicted by velocities varying with time. Gray and green curves represent the Z signal (electroacoustic BAW) and L signal (photoacoustic pulse), respectively. The enlargement shows the signal duration overlap under typical relative phases ($\Delta\varphi = \pm\pi/2$) within the time window of a period (from 0.47 µs to 0.62 µs).

In experiments, the particles are contained in a polydimethylsiloxane (PDMS) microchannel filled with water. PDMS and water have a similar acoustic impedance (plane-wave reflection coefficient $R = 18$ %). In order to reduce simulation time, the simulation domain size is minimized by neglecting acoustic reflections on the PDMS. Instead, a plane-wave radiation boundary condition is used for the Z wave, and a spherical wave radiation boundary condition is used for the L wave. A virtual boundary of radius $R_{\mathrm{VB}} = \sqrt{R_d^2 + h_d^2} + \lambda^Z/2$ shown in Fig. 2(a) is constructed to facilitate the setting of the spherical wave radiation boundary condition. More refined boundary conditions accounting for reflections in the PDMS-water surface and shear waves in the PDMS are discussed by Ni *et al.* [26].

The transducer is not explicitly modeled, instead, the piezoelectric Z excitation is implemented as an r-invariant acceleration:

$$a^Z = a_0^Z \sin\left(\omega^Z t - \varphi^Z\right)\Lambda\left(\frac{\omega^Z t - \varphi^Z}{2\pi}\right). \tag{11}$$

The triangular window $\Lambda(\cdot)$ with the ramp-up range of $[0, n^Z]$ and ramp down of $[n^Z, 2n^Z]$ simulates the resonance onset of the piezoelectric with a train of $n^Z = 5$ cycles, [see Fig. 2(b)]. We note that longer excitation could be possible, but would be more sensitive to reflections at the lateral edge of the wafer that would induce standing waves (and violate the in-plane invariance of the Z wave). The relationship $\omega^L = \omega^Z$ exists unless otherwise specified.

Likewise, the photoacoustic excitation is described by an acceleration with a Gaussian intensity profile, since the photoacoustic vibration is well approximated by a Gaussian profile according to our experimental measurements [27]. We set the radius of the beam waist R_w close to the experimental value (20 μm), producing a normal acceleration given in Eq. (12), where the amplitude reads $a_0^L = v_0^L/\omega^L$. A rectangular window function modulates the sinusoidal signal to simulate the experimentally detected pulsed L signal [see Fig. 2(b)]:

$$\begin{aligned} a^L &= \frac{\partial v_0^L}{\partial t} \\ &= a_0^L e^{-(r/R_w)^2} \frac{\partial}{\partial t}\left[\sin\left(\omega^L t - \varphi^L\right)\Pi\left(\frac{\omega^L t - \varphi^L}{2\pi}\right)\right]. \end{aligned} \tag{12}$$

Here the rectangular window $\Pi(\cdot)$ is set to 1 over the interval $[0, 1/2]$ to simulate a pulse of duration $\tau^L = \pi/\omega^L$ (here $\tau^L = 50$ ns).

A smoothing of 0.4 is used to eliminate frequencies above $f_{\max} = f^Z$ that would trigger numerical instabilities (see Appendix C). The smoothing process introduces small overshoots at the beginning and the end of the laser waveform function with an amplitude negligible compared to the main pulse peak (approximately equal to 20 %). Both excitations have an adjustable phase φ that can be set in experiments using an adjustable delay to a common reference trigger. By default, $\varphi^Z = 0$ and $\varphi^L = (2n^Z + 1/2)\pi$ such that the two excitation waveforms are in phase. When the phase between Z and L is adjusted, φ^Z is the adjustment variable (φ^L remains unchanged) and an empirical reference $\varphi_0(\mathbf{r})$ is introduced such that $\Delta\varphi = \varphi^Z - \varphi_0$ vanishes when the force is 0 at the measurement point $\mathbf{r}$. This is discussed in more detail in Sec. III B 3.

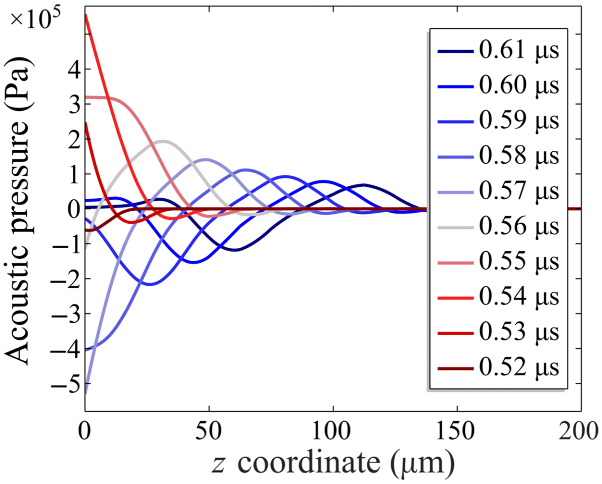

FIG. 3. Acoustic pressure of the L field on the central axis of the simulation domain. As shown in Fig. 2, the laser beam hits the substrate at $t = 0.52$ μs.

III. RESULTS

In this section, we illustrate the working of the laser-guided acoustic tweezers and discuss potential directions for parameter optimization.

A. Acoustic field

As shown in Fig. 2(b), the simulation starts at $t = -0.2t_{\mathrm{sim}} = -0.40$ μs. At $t = 0$, the piezoelectric begins to emit a BAW (Z) wave. The photoacoustic pulse (L signal) hits the substrate at $t = 0.52$ μs. Therefore, the observation of the time evolution starts at $t = 0.52$ μs.

The Z field is a plane traveling wave and remains similar to Fig. 2(b) as it travels in the z direction. The L wave generated by photoacoustic conversion is shown in Fig. 3. It is essentially a spherical wave that behaves similarly in the z and r directions (r profile available in Appendix D). The L-acoustic pressure reaches its maximum amplitude immediately after generation at $t = 0.54$ μs and decays by 80 % by the time it exists in the simulation domain ($t = 0.61$ μs).

B. Acoustic radiation pressure

In manipulation experiments, the particle is confined within the manipulation chamber. Therefore, radial forces tend to be more useful than axial ones. Hence, unless otherwise specified, the ARF will refer to $F_r^{ZL} = -V_p \partial U^{ZL}/\partial r$.

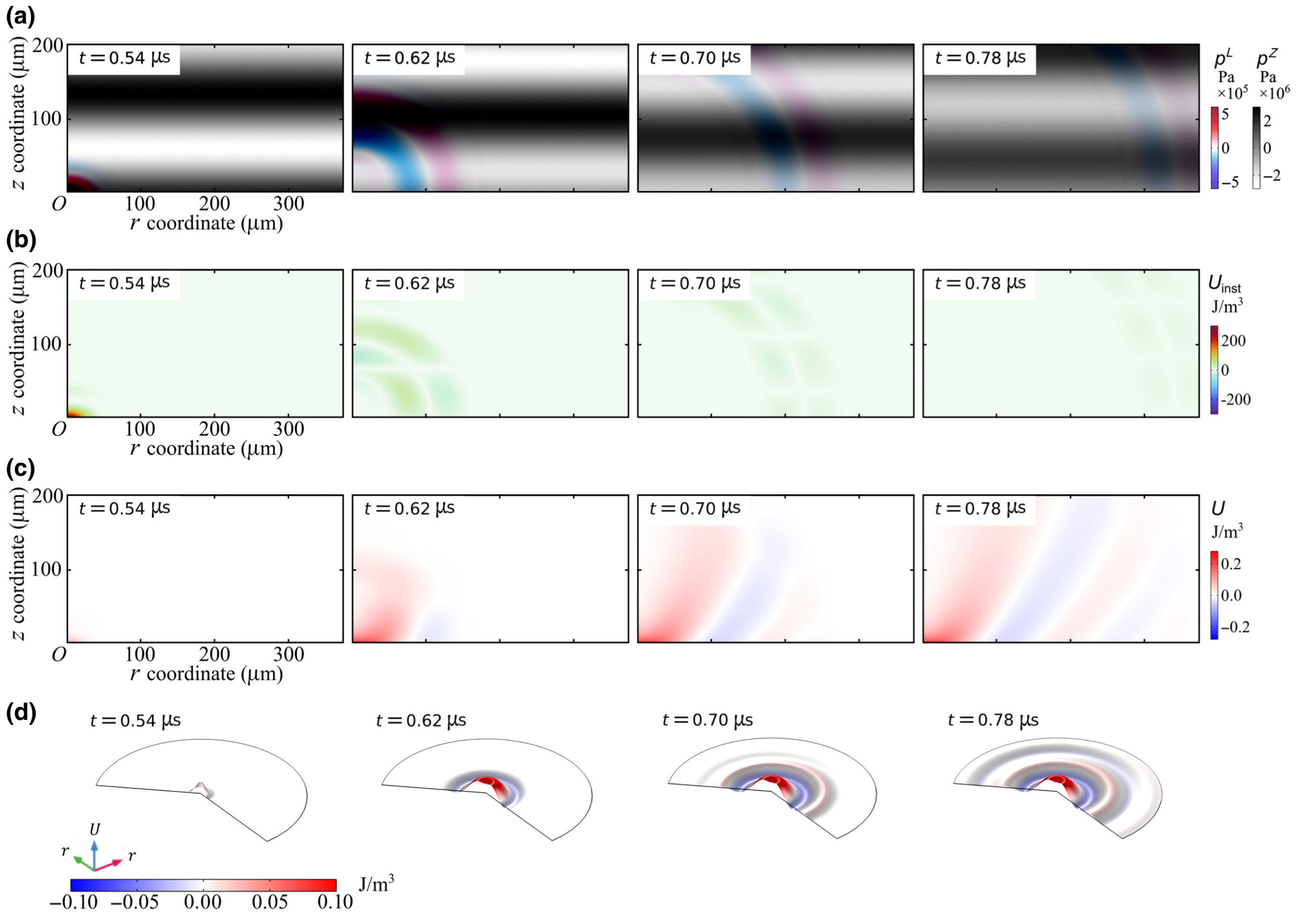

FIG. 4. Time-dependent field evolution with $\Delta\varphi = 0$. Pictures are taken at $t = 0.54$, 0.62, 0.70, and 0.78 μs. (a) Superimposed acoustic pressure field. The blue-red color scale represents the L-field pressure and the white-black color scale represents the Z-field pressure. (b) Instantaneous Gor'kov potential U_{inst}. (c) Time-averaged Gor'kov potential U. (d) Cross section of the magnitude of U at $z = R_p$.

1. Buildup of the Gor'kov potential

Figure 4 shows the buildup of the acoustic radiation pressure. The Z- and L-wave pressures are shown in Fig. 4(a): the Z wave is a traveling plane wave, and the L wave is similar to a spherical wave.

Despite being a virtual quantity, the instantaneous potential U_{inst} to visualize the hybridization of the L and Z fields during the acoustic radiation pressure buildup. For example, the region where $U_{\text{inst}} < 0$ in Fig. 4(b) corresponds to the mixing of p_1^L and p_1^Z of opposite signs. This instantaneous Gor'kov potential grows over time, as shown in Fig. 4(c). As the spherical wave front (L) propagates, the inhomogeneous Gor'kov potential region spreads throughout the entire simulation domain. A cross section of the hybridized Gor'kov potential U^{ZL} experienced by a particle resting on the bottom wall ($z = R_p$) is shown in Fig. 4(d). The potential is mainly concentrated at the location of the laser spot, which ensures good selectivity for acoustic trapping and manipulation. We note that our model neglects the effect of walls, which needs to be accounted for using a more advanced theory (see Ref. [28] for the monofrequency case).

2. Effect of the particle location

The effect of the particle location is shown in Fig. 5, with $\Delta\varphi = \pi/2$ selected to maximize the radiation force (this will be interpreted in Sec. III B 3). The closer the observation position z to the lower edge, the larger the generated ARF peak. The concentration of the pulse energy is also reflected in the ARF curves shown in Figs. 5(a) and 5(b), where the ARF peaks show a decaying trend when moving away from the excitation source either from the r direction or from the z direction. According to Fig. 5, not only does the force become very weak when the particle is located near the top of the channel, but the selectivity (ratio of the primary force maximum to the secondary one) also deteriorates. It is therefore helpful in LGAT design to ensure that the particles are relatively close to the laser spot, which may limit the biocompatibility of the manipulation, unless holographic techniques are used [29]. In the following, the

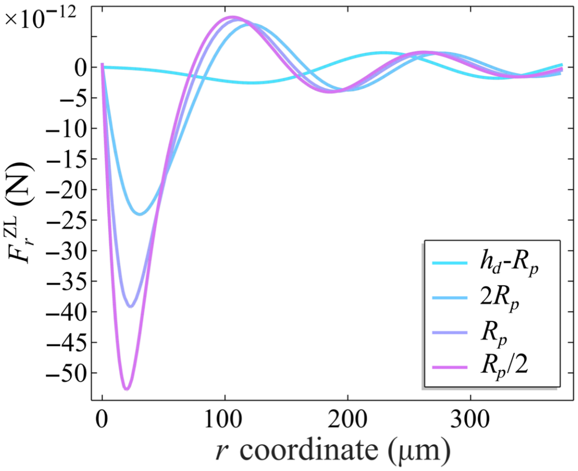

FIG. 5. Variation of the hybridized acoustic radiation force F_r^{ZL} at various heights in the manipulation chamber when $\Delta\varphi = \pi/2$.

force is maximized by assuming that the particle rests at the bottom of the channel ($z = R_p$)

3. *Effect of the phase difference between Z and L fields*

A distinctive feature of LGAT is the possibility to commute between attractive and repelling forces by adjusting the electronic delay between the triggers of the laser source and the electric signal generator. In the simulation, this is implemented by changing the relative phase difference $\Delta\varphi$ between the Z and L fields, as shown for a particle located at $z = R_p = 10\,\mu\text{m}$, $r = 3R_p = 30\,\mu\text{m}$ (Fig. 6). Following a convention proposed in our previous paper, we add an offset $\varphi_0(\mathbf{r})$ to $\Delta\varphi$ such that the ARF cancels for $\Delta\varphi = 0$ [13]. A better alternative will be proposed later on.

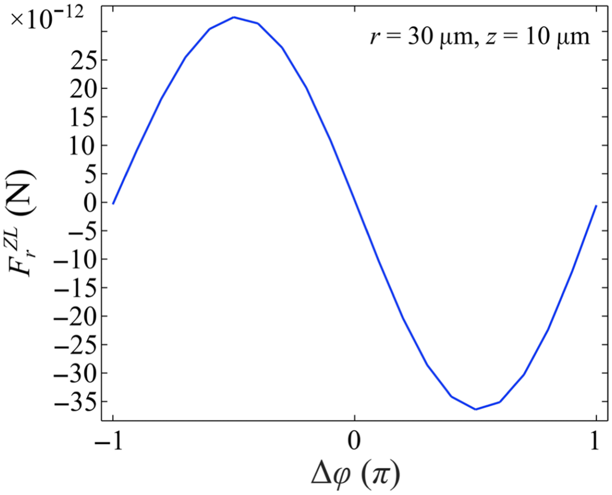

FIG. 6. Hybridized acoustic radiation force F_r^{ZL} at $z = R_p = 10\,\mu\text{m}$, $r = 3R_p = 30\,\mu\text{m}$ depending on the phase difference $\Delta\varphi$ between the Z and L fields.

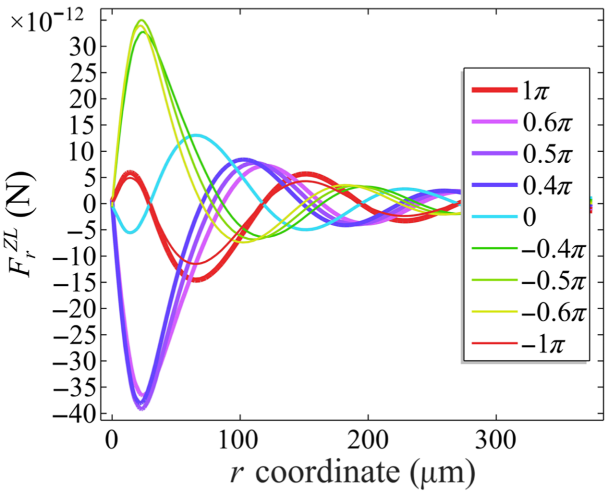

FIG. 7. Variation of the hybridized acoustic radiation force F_r^{ZL} at $z = R_p$ depending on the phase difference $\Delta\varphi$ between the Z and L fields. The line color indicates the phase while the line width grows with the phase in order to visually distinguish between $\Delta\varphi = -\pi$ and $\Delta\varphi = \pi$.

The variation of the ARF at fixed $z = R_p = 10\,\mu\text{m}$ but with a varying phase is shown in Fig. 7. Here, the phase offset is kept at 0 so that $\Delta\varphi = \varphi^Z$ everywhere. Although at $r = 3R_p = 30\,\mu\text{m}$ the force behaves consistently with Fig. 6 (strongest pull at $\Delta\varphi = \pi/2$, strongest push at $\Delta\varphi = -\pi/2$, and vanishingly small at $\Delta\varphi = 0$), it can be seen that points at half a wavelength away (such as $r = 105\,\mu\text{m}$) behave in the opposite fashion and points a quarter wavelength away (such as $r = 62\,\mu\text{m}$) behave in phase quadrature (strongest pull at $\Delta\varphi = \pi$, strongest push at $\Delta\varphi = 0$ and vanishingly small at $\Delta\varphi = \pm\pi/2$). This demonstrates that the exact delay between the L and Z fields depends not only on the triggers of the instruments, but also on the acoustic propagation of both fields. The latter is relative to the exact point in space where the ARF is measured. This issue is addressed in the next section. We also note that the force is not exactly periodic over time due to the slow variations of the wave envelope (the wave amplitude is not the same for $\Delta\varphi = -\pi$ and $\Delta\varphi = \pi$).

4. *A phase-independent factorization of the hybridized Gor'kov potential*

In the previous section, we show that the phase difference $\Delta\varphi$ is a useful factor controlling the ARF of LGAT, but that the relationship between the force direction and $\Delta\varphi$ depends on the spatial location of the particle being manipulated. Hence, gaining a perfect knowledge of the ARF of a LGAT would require repeating the ARF calculations for all phases $\Delta\varphi \in [-\pi, \pi]$. Here, we show how to reduce this large number of calculations to only two. Reference [13] gives a way to obtain the hybridized potential U^{ZL} by setting up an analytical Z-field wave with constant amplitude. Then U^{ZL} is expressed as a linear combination of two basis potentials weighted by trigonometric functions of $\Delta\varphi$:

$$\hat{U}^{ZL} = U_c \cos\Delta\varphi + U_s \sin\Delta\varphi, \tag{13}$$

with the basis potentials $U_c(\mathbf{r}) = \langle p_1^Z|_{\Delta\varphi=0} E^L\rangle$ and $U_s(\mathbf{r}) = \langle p_1^Z|_{\Delta\varphi=\pi/2} E^L\rangle$ independent of $\Delta\varphi$, with the L component $E^L = f_1 p_1^L/(\rho_0 c_0^2) - (3/2) f_2 v_{1z}^L/c_0$. Here, only the z-direction component of $\mathbf{v}_1^L$ is considered due to z-propagating-only $\mathbf{v}_1^Z$. $\hat{U}^{ZL}$ obtained from Eq. (13) is strictly valid only for the monofrequency Z wave but is assumed here to be a good approximation of the actual potential U^{ZL}. In the simulations, U_c (U_s) is obtained by setting $\Delta\varphi = 0$ ($\Delta\varphi = \pi/2$). The approximate potential can then be computed from these two basis potentials according to Eq. (13).

Figure 8(a) shows the basis potentials at $z = R_p$. Their values can be recorded in the entire simulation domain. The quality of the approximation is evaluated in Fig. 8(b): the approximated potential matches U^{ZL} [from Eq. (3)] well, although the relative error for $\Delta\varphi = -\pi$ increases to approximately 8 % compared to that of $\Delta\varphi = \pi/10$. This is probably because the Z wave has a triangular envelope of varying amplitude, which is not considered in the theory of Ref. [13].

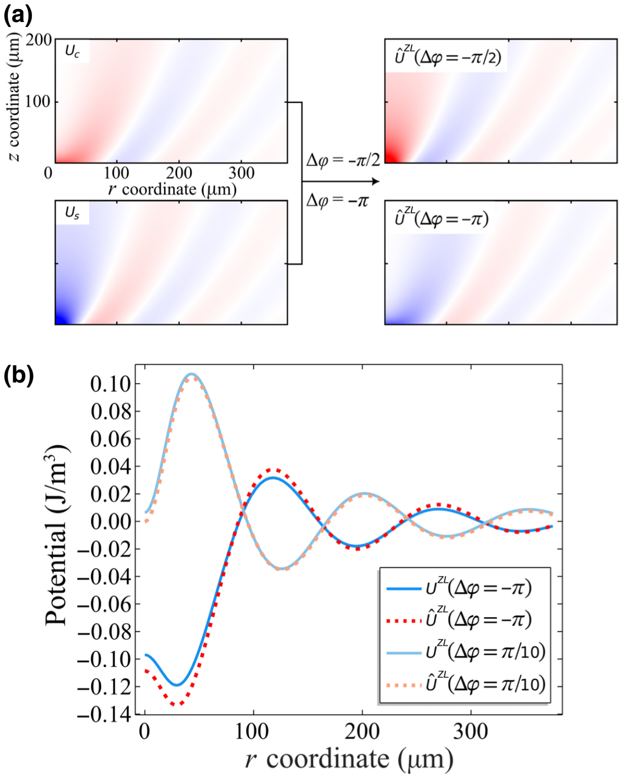

FIG. 8. Approximate Gor'kov potential $\hat{U}^{ZL}$ with $\Delta\varphi$ decoupled. (a) Constant basis potentials U_c and U_s. (b) Comparison between $\hat{U}^{ZL}$ and U^{ZL} for $\Delta\varphi = -\pi$ and $\pi/10$.

C. Optimization of operating parameters

The main weakness of current LGAT implementations is that they provide a very small force, which results in displacement velocities of only a few micrometers per second. In the following, we optimize two parameters readily adjustable in experiments: (1) the ratio of the L-wave frequency (reflecting the laser pulse duration) with respect to the Z-wave frequency, i.e., $\xi_f = f^L/f^Z$ (which can be adjusted on most pulsed-laser sources); (2) the size of the pulse source, expressed as the radius of the laser spot R_b (which can be adjusted by changing the magnification of the microscope objective). We assume that ξ_f is adjusted by changing f^L with f^Z fixed at 10 MHz. In this section, the conditions $\Delta\varphi = \pi/2$ and $z = R_p$ are retained, and the radiation force magnitude $F_r{}^{\max}$ is discussed based on the maximum absolute values of the ARF in the r direction.

To reflect experimental constraints, the comparisons are done at constant peak laser energy (which would be equivalent to adjusting the laser energy to avoid material damage). Photoacoustic generation theory shows that the photoacoustic wave amplitude is proportional to the laser power. Therefore, we adjust the photoacoustic wave amplitude as $v_0^L(\xi_f) = \xi_f v_0^L(\xi_f = 1)$ (see Appendix E). In addition, the laser phase φ^L is adjusted to keep the peak synchronized with the electroacoustic field peak.

Figure 9 illustrates the effect of modulating ξ_f on the ARF. The ARF increases rapidly as the pulse shortens until it reaches a saturation value of $F_r{}^{\max} \sim 44$ pN when the pulse frequency satisfies ($f^L \sim f^Z$). After that, the

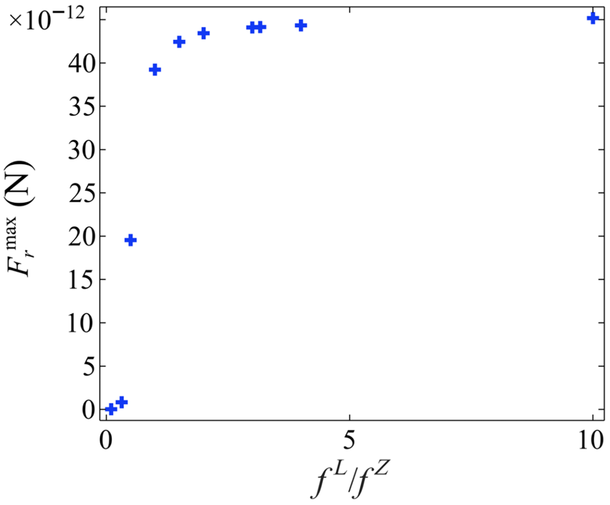

FIG. 9. Hybridized acoustic radiation force $F_r^{\max}$ for various pulse durations (f^L/f^Z) while keeping the laser pulse energy constant.

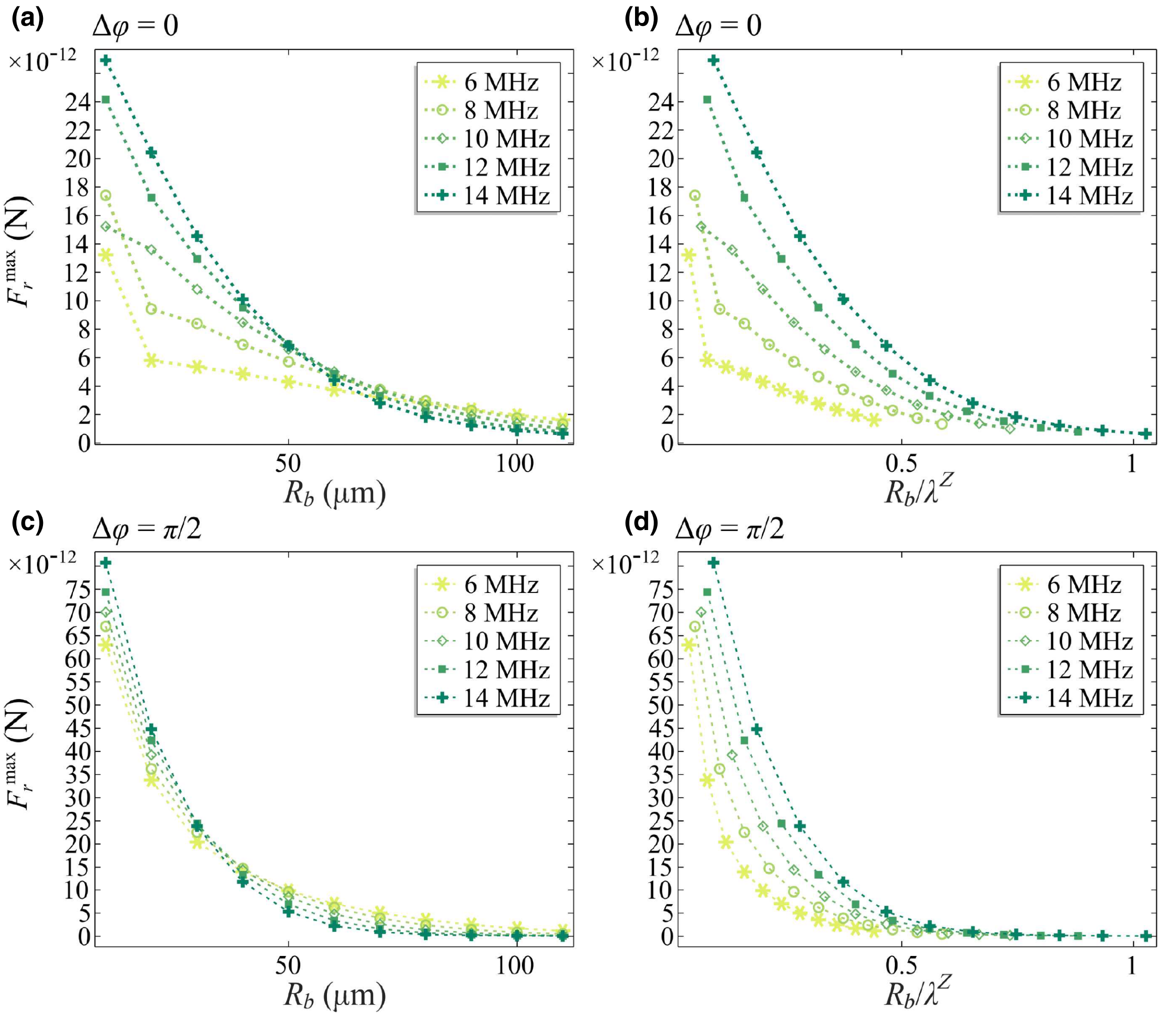

FIG. 10. Hybridized acoustic radiation force $F_r^{\max}$ for various pulse durations (expressed as frequencies of 6, 8, 10, 12, and 14 MHz) and beam radii, while keeping the beam energy constant. (a),(b) present the force versus the beam radius R_b and the dimensionless radius R_b/λ^Z for $\Delta\varphi = 0$ while (c),(d) present those for $\Delta\varphi = \pi/2$.

increase flattens out. While the marginal improvement after $f^L \sim f^Z$ may seem attractive for improved versions of the LGAT, we note that the short wavelength at high frequencies violates Gor'kov's assumption of an object size much smaller than the wavelength, and the onset of resonance may lead to a force direction that changes rapidly with the particle size, making it unpredictable unless both the particle size and the acoustic field are known precisely in advance.

Next, we consider varying the laser spot size, for instance, by using microscope objectives of varying magnifications. Here, R_b is introduced to distinguish the adjusted spot radius from the original radius R_w used in other parts of the paper. The ratio $\xi_R = R_b/R_w$ is defined for convenience. To maintain pulse energy constant, the scaling $v_0^L(\xi_R) = v_0^L(\xi_R = 1)/\xi_R^2$ neglecting the transmission loss of high-magnification objectives is used (detailed derivation in Appendix E).

Figures 10(a) and 10(b) show the evolution of the ARF depending on the pulse source radius when $\Delta\varphi = 0$ and Figs. 10(c) and 10(d) show the evolution of the ARF depending on the pulse source radius when $\Delta\varphi = \pi/2$. It is found that $\Delta\varphi = \pi/2$ yields the largest force regardless of the frequency and beam radius. By optimizing the latter two parameters [$f^L = 14$ MHz (pulse duration of 31 ns), $R_b = 10\,\mu$m], we expect a force of approximately 80 pN, well within the range of other acoustic tweezers, but with the extra advantage of being controlled by a light pattern.

IV. PERSPECTIVE

So far, the model is limited to the case of small particles in an ideal fluid domain, and the properties of the wave sources are relatively simplified. Therefore, the model could benefit from further extensions, such as the introduction of thermoviscous effects and interaction with walls. Furthermore, we assume in the model that the radius of the particle is small enough to be consistent with the Gor'kov approximation [30]. However, the LGAT experiments [13] manipulating particles with approximately 25 μm have unveiled a much larger force, presumably due to the onset of resonance. Therefore, a theory for transient ARF valid for arbitrary particle radii would be highly desirable.

V. CONCLUSION

Despite the availability of a theoretical expression for the ARF of short pulses and wave trains, no finite-element models have been implemented so far. In this paper, we show that such a simulation could be carried out by (i) using time-explicit acoustic pressure simulations to compute the acoustic field, (ii) defining a virtual instantaneous Gor'kov potential, and (iii) integrating it over time to obtain the time-averaged Gor'kov potential. We then use our code to simulate LGATs. Our simulations show that the behavior of the LGAT can be captured by two conjugated Gor'kov potentials U_c and U_s weighted by trigonometric functions. Optimization of the operating parameters shows that the force increases as the laser spot size is reduced, while the gain from shortening the pulse duration is limited (approximately 10 %). Finally, based on the dielectric breakdown limit of the piezoelectric, we estimate the maximum LGAT force on 10 μm polystyrene particles in water to be approximately 80 pN, which is comparable to other acoustic tweezers. Beyond LGAT, the availability of a numerical model may accelerate the development of time-dynamic acoustic tweezers with superior dexterity compared to their monochromatic counterparts.

ACKNOWLEDGMENTS

This work is supported by the National Natural Science Foundation of China with Grants No. 62274039 and No. 12004078; the State Key Lab of ASIC and System, Fudan University with Grants No. 2021MS001, No. 2021MS002, and No. 2020KF006; and the Science and Technology Commission of Shanghai Municipality with Grants No. 22QA1400900 and No. 22WZ2502200.

APPENDIX A: CONVERGENCE ANALYSIS OF THE MESH SETUP

The maximum and mesh element sizes are directly controlled by N, the number of elements per local wavelength. To examine the accuracy of the mesh setup after gradual refinement, N is set to 2, 6, 12, and 18, respectively ($N = 12$ is used in our simulations). The ARF F_r^{ZL} at $z = R_p$ with $\Delta\varphi = \pi/2$ is chosen as the metric. As shown in Fig. 11, the result overlapping from $N = 6$ to $N = 18$ shows good convergence of the mesh setup, except for $N = 2$, where the results show significant deviations due to the overly coarse mesh.

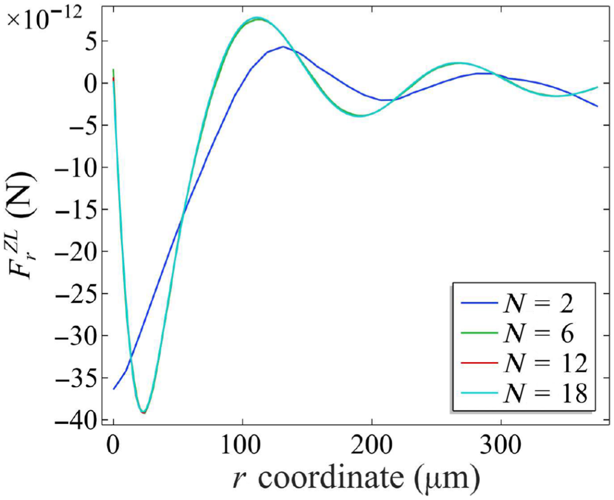

FIG. 11. Comparison of F_r^{ZL} on $z = R_p$ with $\Delta\varphi = \pi/2$ when the mesh is discretized by different values of N.

APPENDIX B: MAGNITUDE COMPARISON BETWEEN U^{LL} AND U^{ZL}

The simulation method follows the hypothesis of the hybridized-field theory [13], which expects a relatively low value of U^{LL} compared to U^{ZL}. U^{LL} is independent of $\Delta\varphi$. Here we evaluate the effect of U^{LL} with the maximum U^{ZL} induced by adjusting $\Delta\varphi$.

As shown in Fig. 12, the maximum U^{LL} reaches less than 10 % of the maximum U^{ZL}, which validates our assumption for the current simulation settings.

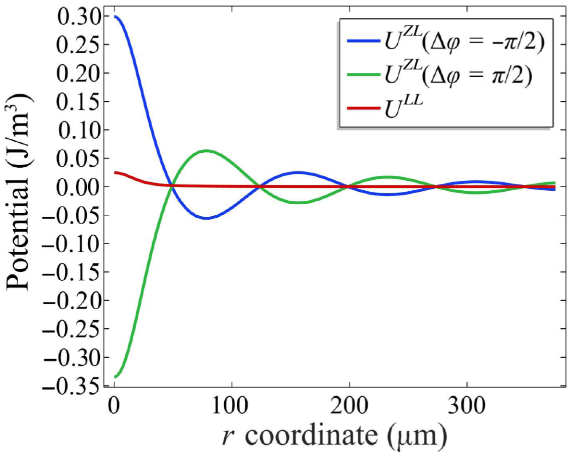

FIG. 12. Magnitude comparison between U^{LL} and U^{ZL} with $\Delta\varphi = \pm\pi/2$.

APPENDIX C: EFFECTS OF INPUT SIGNAL SMOOTHING

Since the acceleration a^L is obtained by deriving the velocity, the discontinuities at the beginning and the end of the signal result in sharp variations [as shown in Fig. 13(a)]. These large changes tend to generate numerical errors. To minimize this issue, we introduce a transition region of width $0.4\omega^L/2\pi$ on each side of the rectangular window. In Fig. 13(b), we check that the deviation of the ARF resulting from the smoothing is moderate when compared to the nonsmoothed function.

APPENDIX D: ISOTROPY OF THE LASER PULSE

The photogenerated L wave is nearly a spherical wave. The acoustic field in the r direction (Fig. 14) and in the z direction (Fig. 3) are almost similar. However, in the near-field region, the acoustic pressure change in the r direction is sharper due to the normal direction of the initial acceleration.

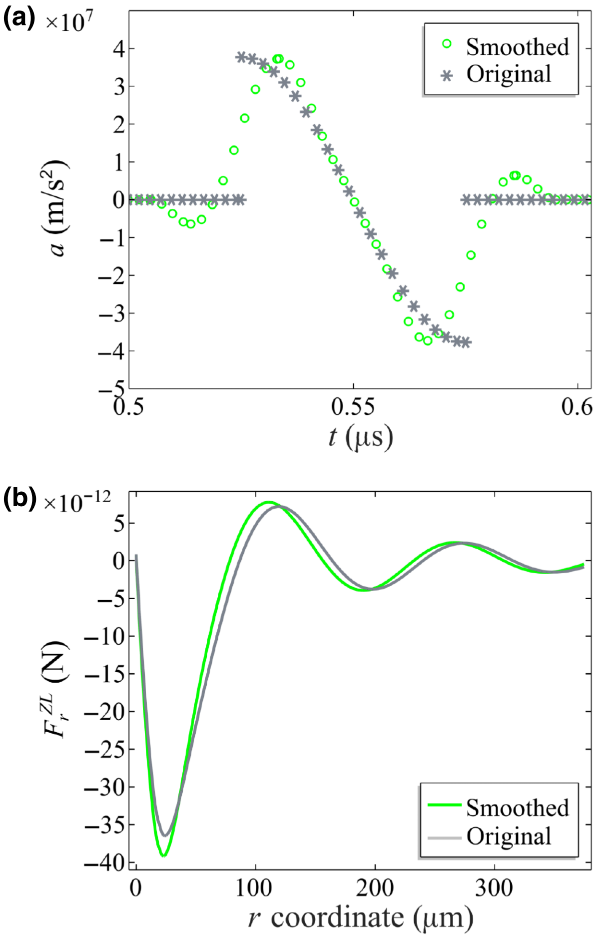

FIG. 13. Comparison between the sharp signal and the smoothed signal. (a) Signal input. (b) F_r^{ZL} on $z = R_p$ with $\Delta\varphi = \pi/2$.

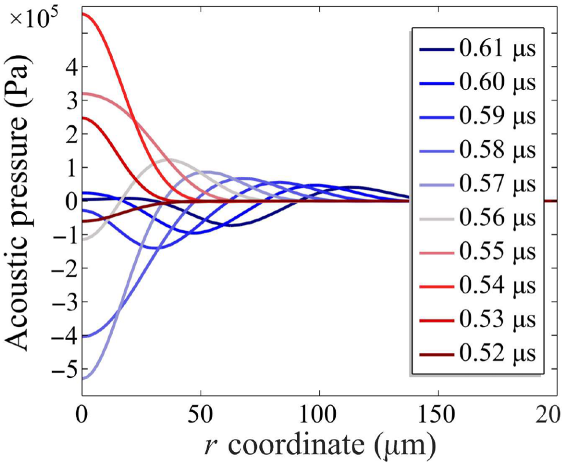

FIG. 14. Propagating properties of the L-acoustic pressure varying with r on the lower edge ($z = 0$). The color bar from red to blue represents the time change from 0.52 μs to 0.61 μs.

APPENDIX E: SCALING OF THE VELOCITY TO MAINTAIN A CONSTANT LASER PULSE ENERGY

When changing the operating parameters in the simulations, the laser pulse energy is assumed to remain constant. This is achieved by scaling the L velocity according to the Vashy-Buckingham Π theorem. The velocity is assumed to read

$$v^L(f^L t, r/R_b) = v_0^L(\xi_R, \xi_f) g(f^L t, r/R_b), \tag{E1}$$

where g is an arbitrary integrable function that can be obtained in our simulations by integrating Eq. (12). The goal of the following calculation is to determine $v_0^L(\xi_R, \xi_f)/v_0^L(1,1)$.

The pulse energy from the laser reads $E = \int_{A_{\mathrm{tot}}}\int_{t_{\mathrm{tot}}} \varepsilon\, \mathrm{d}S\mathrm{d}t$, where ε is the pulse power density. Substituting $\varepsilon = \beta^{-1} v^L$, with β the photoacoustic conversion coefficient (assumed to be constant for the limited frequency and power range studied here), and using Eq. (E1), we get

$$E \approx \beta^{-1} v_0^L(\xi_R, \xi_f) \int_\infty \int_\infty g(f^L t, r/R_b)\mathrm{d}S\mathrm{d}t. \tag{E2}$$

The right-hand side integral is obtained by assuming that the simulation domain is large enough to completely encompass the laser spot. Changing the integration variables to $f^L t$ and r/R_b, we get

$$E \approx \beta^{-1} v_0^L(\xi_R, \xi_f) \frac{{R_b}^2}{f^L} I_g, \tag{E3}$$

where I_g is the definite integral of the g function.

A similar development at $(\xi_R, \xi_f) = (1, 1)$ yields

$$E \approx \beta^{-1} v_0^L(1,1) \frac{{R_w}^2}{f^Z} I_g, \tag{E4}$$

which yields $v_0^L(\xi_R, \xi_f)/v_0^L(1,1) = \xi_f/{\xi_R}^2$ that is used in the simulations.

[1] S. Li, X. Ding, Z. Mao, Y. Chen, N. Nama, F. Guo, P. Li, L. Wang, C. E. Cameron, and T. J. Huang, Standing surface acoustic wave (SSAW)-based cell washing, Lab Chip **15**, 331 (2015).

[2] R. Ahmad, G. Destgeer, M. Afzal, J. Park, H. Ahmed, J. H. Jung, K. Park, T.-S. Yoon, and H. J. Sung, Acoustic wave-driven functionalized particles for Aptamer-based target biomolecule separation, Anal. Chem. **89**, 13313 (2017).

[3] P. Dow, K. Kotz, S. Gruszka, J. Holder, and J. Fiering, Acoustic separation in plastic microfluidics for rapid detection of bacteria in blood using engineered bacteriophage, Lab Chip **18**, 923 (2018).

[4] M. Antfolk, C. Magnusson, P. Augustsson, H. Lilja, and T. Laurell, Acoustofluidic, label-free separation and simultaneous concentration of rare tumor cells from white blood cells, Anal. Chem. **87**, 9322 (2015).

[5] P. Augustsson, J. T. Karlsen, H.-W. Su, H. Bruus, and J. Voldman, Iso-acoustic focusing of cells for size-insensitive acousto-mechanical phenotyping, Nat. Commun. **7**, 11556 (2016).

[6] L. Schmid, D. A. Weitz, and T. Franke, Sorting drops and cells with acoustics: acoustic microfluidic fluorescence-activated cell sorter, Lab Chip **14**, 3710 (2014).

[7] M. Baudoin, J.-L. Thomas, R. A. Sahely, J.-C. Gerbedoen, Z. Gong, A. Sivery, O. B. Matar, N. Smagin, P. Favreau, and A. Vlandas, Spatially selective manipulation of cells with single-beam acoustical tweezers, Nat. Commun. **11**, 4244 (2020).

[8] M. Hoyos and A. Castro, Controlling the acoustic streaming by pulsed ultrasounds, Ultrasonics **53**, 70 (2013).

[9] A. Castro and M. Hoyos, Study of the onset of the acoustic streaming in parallel plate resonators with pulse ultrasound, Ultrasonics **66**, 166 (2016).

[10] C. Goering and J. Dual, Dynamic measurement of the acoustic streaming time constant utilizing an optical tweezer, Phys. Rev. E **104**, 025104 (2021).

[11] C. Goering and J. Dual, Measuring the effects of a pulsed excitation on the buildup of acoustic streaming and the acoustic radiation force utilizing an optical tweezer, Phys. Rev. E **105**, 055103 (2022).

[12] D. J. Collins, C. Devendran, Z. Ma, J. W. Ng, A. Neild, and Y. Ai, Acoustic tweezers via sub–time-of-flight regime surface acoustic waves, Sci. Adv. **2**, e1600089 (2016).

[13] Q. Wang, S. Chen, J. Zhou, and A. Riaud, Laser-guided acoustic tweezers, arXiv:2203.14497 (2022).

[14] P. B. Muller and H. Bruus, Theoretical study of time-dependent, ultrasound-induced acoustic streaming in microchannels, Phys. Rev. E **92**, 063018 (2015).

[15] J. Voß and R. Wittkowski, On the shape-dependent propulsion of nano- and microparticles by traveling ultrasound waves, Nanoscale Adv. **2**, 3890 (2020).

[16] A. L. Longhorn, The unsteady, subsonic motion of a sphere in a compressible inviscid fluid, Q. J. Mech. Appl. Math. **5**, 64 (1952).

[17] L. P. Gor'kov, Forces acting on a small particle in an acoustic field within an ideal fluid, Dokl. Akad. Nauk SSSR **140**, 88 (1961).

[18] Q. Wang, A. Riaud, J. Zhou, Z. Gong, and M. Baudoin, Acoustic Radiation Force on Small Spheres Due to Transient Acoustic Fields, Phys. Rev. Appl. **15**, 044034 (2021).

[19] T. Baasch, A. Pavlic, and J. Dual, Acoustic radiation force acting on a heavy particle in a standing wave can be dominated by the acoustic microstreaming, Phys. Rev. E **100**, 061102(R) (2019).

[20] M. Settnes and H. Bruus, Forces acting on a small particle in an acoustical field in a viscous fluid, Phys. Rev. E **85**, 016327 (2012).

[21] J. T. Karlsen and H. Bruus, Forces acting on a small particle in an acoustical field in a thermoviscous fluid, Phys. Rev. E **92**, 043010 (2015).

[22] COMSOL Multiphysics® Support Knowledge Base: Resolving time-dependent waves, https://www.comsol.com/support/knowledgebase/1118, last accessed date: May 8, 2023.

[23] R. Barnkob, P. Augustsson, T. Laurell, and H. Bruus, Acoustic radiation- and streaming-induced microparticle velocities determined by microparticle image velocimetry in an ultrasound symmetry plane, Phys. Rev. E **86**, 056307 (2012).

[24] W. Qiu, J. H. Joergensen, E. Corato, H. Bruus, and P. Augustsson, Fast Microscale Acoustic Streaming Driven by a Temperature-Gradient-Induced Nondissipative Acoustic Body Force, Phys. Rev. Lett. **127**, 064501 (2021).

[25] L. E. Myers, G. D. Miller, R. C. Eckardt, M. M. Fejer, R. L. Byer, and W. R. Bosenberg, Quasi-phase-matched 1.064-μm-pumped optical parametric oscillator in bulk periodically poled $\mathrm{LiNbO_3}$, Opt. Lett. **20**, 52 (1995).

[26] Z. Ni, C. Yin, G. Xu, L. Xie, J. Huang, S. Liu, J. Tu, X. Guo, and D. Zhang, Modelling of SAW-PDMS acoustofluidics: physical fields and particle motions influenced by different descriptions of the PDMS domain, Lab Chip **19**, 2728 (2019).

[27] Q. Wang, J. Zhou, X. Wu, and A. Riaud, Optimization of the synthesis conditions of gold nanoparticle–polydimethylsiloxane composites for ultrasound generation, Mater. Adv. **3**, 2850 (2022).

[28] T. Baasch and J. Dual, Acoustic Radiation Force on a Spherical Fluid or Solid Elastic Particle Placed Close to a Fluid or Solid Elastic Half-Space, Phys. Rev. Appl. **14**, 024052 (2020).

[29] T. Wei, H. Guo, J. Lu, X. Huang, W. Deng, F. Li, and Z. Liu, Generating arbitrary photoacoustic fields with a spatial light modulator, Opt. Lett. **44**, 3206 (2019).

[30] T. Hasegawa, Comparison of two solutions for acoustic radiation pressure on a sphere, J. Acoust. Soc. Am. **61**, 1445 (1977).